Journal of The Electrochemical Society, **166** (12) F796-F804 (2019)
0013-4651/2019/166(12)/F796/9/$38.00 © The Electrochemical Society

Positive Effect of Incorporating $Er_{0.4}Bi_{1.6}O_3$ on the Performance and Stability of $La_2NiO_{4+\delta}$ Cathode

Zelong He,[1] Na Ai,[2,3] Shuai He,[4] San Ping Jiang,[4] Lan Zhang,[5] William D. A. Rickard,[6] Dian Tang,[2] and Kongfa Chen[2,z]

[1] *School of Electronic and Information Engineering, Yangtze Normal University, Chongqing 408100, China*
[2] *College of Materials Science and Engineering, Fuzhou University, Fuzhou, Fujian 350108, China*
[3] *Testing Center, Fuzhou University, Fuzhou, Fujian 350108, China*
[4] *Fuels and Energy Technology Institute and Department of Chemical Engineering, Curtin University, Perth WA 6102, Australia*
[5] *Energy Research Institute @ NTU, Nanyang Technological University, Singapore 637553, Singapore*
[6] *John De Laeter Centre & Department of Physics and Astronomy, Curtin University, Perth, WA 6102, Australia*

Layered Ruddlesden-Popper $La_2NiO_{4+\delta}$ (LNO) is reported to possess excellent oxygen surface and bulk transport properties, but its application as the cathode of solid oxide fuel cells is restrained by the relatively poor electrocatalytic activity. Here, we report the incorporation of highly ion-conducting Er-stabilized Bi_2O_3 (ESB) into LNO and assemble the LNO-ESB composite cathode directly on zirconia electrolyte film using a facile electrochemical polarization approach. The results show the presence of ESB remarkably reduces the contact resistance at the electrode/electrolyte interface and enhances the electrocatalytic activity and cation stability of LNO. The cell with the LNO-ESB cathode generates a peak power density of 852 mW cm^{-2} at 750°C with reasonable operating stability over 200 h. This work demonstrates the feasibility of incorporating ESB to promote the layered nickelate cathodes for intermediate temperature solid oxide fuel cells.
© 2019 The Electrochemical Society. [DOI: 10.1149/2.0841912jes]

Manuscript submitted May 16, 2019; revised manuscript received July 8, 2019. Published July 17, 2019.

Solid oxide fuel cells (SOFCs) are one of the cleanest and most efficient all-solid devices to directly convert the chemical energy of a variety of fuels to electrical power. The development of high performance SOFCs is critically hindered by the sluggish kinetics of oxygen reduction reaction (ORR) at the cathode side, which however is dramatically dependent on the type of cathode materials.[1–3] K_2NiF_4-type layered Ruddlesden-Popper $La_2NiO_{4+\delta}$ (LNO) exhibits excellent oxygen surface exchange and bulk transport properties, and therefore, is regarded as a promising cathode material for intermediate temperature SOFCs (IT-SOFCs).[4–6] For example, LNO has an oxgyen surface exchange coefficient (k) of 2.55×10^{-6} cm s^{-1} and an oxygen tracer diffusion coefficient (D^*) of 1.71×10^{-7} cm^2 s^{-1} at ~800°C, higher than the state-of-the-art mixed ionic and electronic conductor $La_{0.6}Sr_{0.4}Co_{0.2}Fe_{0.8}O_{3-\delta}$ (LSCF).[5] The decoration of a LNO layer on the surfaces of LSCF,[7,8] $Ba_{0.5}Sr_{0.5}Co_{0.8}Fe_{0.2}O_{3-\delta}$[9] and $PrBa_{0.5}Sr_{0.5}Co_{1.5}Fe_{0.5}O_{5+\delta}$[10] not only enhances the electrocatalytic activity for ORR, but also promotes the structural stability of the cathodes against the attack by volatile contaminants such as chromium, sulfur and carbon dioxide. The positive effect of the LNO layer is attributed to the absence of alkaline earth metals in particular strontium, which are a nucleating agent in initiating the interaction with the contaminants.[1,11,12] Compared with the cobalt-containing cathodes with a high thermal expansion coefficient (TEC), LNO possesses a moderate TEC of 13.7×10^{-6} K^{-1}, making it more thermally compatible with commonly used Y_2O_3-stabilized ZrO_2 (YSZ) and Gd-doped CeO_2 (GDC) electrolytes.[4,5]

However, literature survey indicates that LNO as a cathode of SOFCs virtually exhibits relatively poor electrocatalytic activity for ORR. Skinner's group reported that the electrode polarization resistance of a LNO electrode was as high as 7.4 Ω cm^2 at 700°C.[13] Escudero et al. fabricated a cell with Ni-$Sm_{0.2}Ce_{0.8}O_{1.9}$ (SDC) anode/SDC/$La_{0.9}Sr_{0.1}Ga_{0.8}Mg_{0.2}O_{2.85}$ electrolyte/LNO cathode and obtained peak power densities (PPDs) of 160 and 226 mW cm^{-2} at 750 and 800°C, respectively.[14] Fondard et al.'s metal-supported cell with a structure of Ni-YSZ anode/YSZ film/GDC layer/LNO cathode generated a PPD in the range of 60–76 mW cm^{-2} at 700°C.[15] As a consequence, there are numerous efforts motivating to enhance the electrocatalytic performance of LNO electrodes. This includes the design of a nanostructured LNO-based cathode,[16–19] doping of cations such as Pr and Bi in the La-site and Mn, Co, Cu and Fe in the Ni-site,[20–23] construction of a multilayer structure such as a compact LNO inner layer/porous LNO outer layer[13,24,25] and a LNO compact inner layer/LNO-$La_4Ni_3O_{10-\delta}$ ($L_4N_3O_{10}$) composite middle layer/$L_4N_3O_{10}$ outer layer,[26] and combination with a second phase to form a composite such as LNO-$L_4N_3O_{10}$,[27] LNO-$LaNi_{0.6}Fe_{0.4}O_{3-\delta}$[28] and LNO-doped ceria.[29,30]

Cubic bismuth oxide (δ-Bi_2O_3) is highly ion conductive with superb oxygen surface exchange ability.[31] The addition of Y and Er-stabilized Bi_2O_3 (YSB and ESB) remarkably promotes the electrocatalytic activity of cathodes such as $La_{0.8}Sr_{0.2}MnO_{3+\delta}$ (LSM), LSCF and $Sm_{0.95}Co_{0.95}Pd_{0.05}O_{3-\delta}$.[32–41] However, to our best knowledge there are rare reports regarding the incorporation of stabilized Bi_2O_3 to LNO. Here, we aim to modify LNO by ESB and anticipate the ESB phase would lead to performance promotion of LNO. We attempt to assemble the LNO-ESB electrode on barrier-layer-free YSZ electrolyte using an electrochemical polarization approach without the conventional electrode sintering process at 1000–1200°C. This is based on our recent findings that the electrode/electrolyte interface can be in situ formed via the electrochemical polarization under the operating conditions of SOFCs (700-800°C).[42–46] The electrochemical polarization assisted electrode fabrication is benign to avoid the potential chemical reaction at the interface between LNO and YSZ at a temperature of 900°C and above.[47–49] The results show that compared to the pristine LNO electrode, the LNO-ESB composite electrode exhibits a remarkably reduced interfacial contact resistance as well as enhanced electrocatalytic activity and operating stability.

Experimental

Preparation of electrode powder and ink.—$La_2NiO_{4+\delta}$ (LNO) and $Er_{0.4}Bi_{1.6}O_3$ (ESB) powders were synthesized via a sol-gel route, using $La(NO_3)_3{\cdot}6H_2O$ (99.9%), $Ni(NO_3)_2{\cdot}9H_2O$ (98%), $Er(NO_3)_3{\cdot}5H_2O$ (99.9%), $Bi(NO_3)_3{\cdot}5H_2O$ (98%), citric acid (99.5%), ethylenediaminetetraacetic acid (EDTA, 99%) and ammonia solution (28%). The LNO and ESB gels were calcined at 900 and 600°C for 3 h, respectively. LNO and ESB were mixed in 60:40 by mass, and the mixture was blended with an ink vehicle (4 wt% ethyl cellulose + 96 wt% terpineol) in 70:30 by mass. Pristine LNO ink was also prepared for comparison. To perform chemical compatibility analysis, LNO and YSZ (TZ-8Y, Tosoh) powders were mixed in 50:50 by mass and calcined at 800–900°C for 4 h.

Preparation and testing of single cells.—Anode substrate/14 μm anode functional layer (AFL)/12 μm YSZ film cells were

[z]E-mail: kongfa.chen@fzu.edu.cn

prepared using a slurry spin coating approach. The details are available elsewhere.[50,51] The anode substrates consisted of NiO (J.T. Baker), YSZ and tapioca starch of 40:40:20 in mass, and AFL of NiO and YSZ of 50:50 in mass. The supported YSZ films were fired at 1450°C for 5 h. LNO and LNO-ESB inks were screen-printed on the YSZ films with a geometric area of 0.23 cm^2 and heat-treated at 150°C for 2 h. No further electrode sintering processes were performed.

The single cells were sealed on ceramic tubes and heated up to 750°C, where the anodes were reduced in hydrogen at a flow rate of 50 ml min^{-1}. Electrochemical polarization curves and impedance spectra were measured at 600–750°C, using a Gamry Potentiostat (Reference 3000 and Interface 1000E). The cells' operating stability was conducted under a constant current density of 0.1 and 0.5 A cm^{-2} at 750°C. The frequency range for measuring impedance spectra was 100 kHz–0.1 Hz and AC signal amplitude was 10 mV.

Phase and microstructure characterizations.—The crystal phases of LNO, ESB powders and calcined LNO-YSZ mixtures were characterized using an X-ray diffractometer (XRD, Bruker D8 Advance and Rigaku Miniflex600) with a Cu Kα X-ray source. The morphology and elemental analysis of LNO powder as well as LNO and LNO-ESB electrodes were characterized using a scanning electron microscope (SEM, Zeiss Neon 40EsB and Supra55 Sapphire) equipped with energy dispersive spectroscopy (EDS). The electrodes were partly peeled off to expose the electrolyte surfaces using an adhesive tape approach, and the elemental distribution on the electrolyte surfaces (10 μm × 10 μm region) was probed with a Tescan Lyra FIB-SEM with a Tofwerks Time of flight secondary ion mass spectrometer (ToF-SIMS) using an ion beam accelerating voltage of 30 kV and current of 35 pA. Positive ions were detected during the SIMS tests.

Results and Discussion

Phase and microstructure.—Figure 1a shows the XRD patterns and SEM image of as synthesized LNO powder. The LNO powder exhibits a typical tetragonal structure after calcination at 900°C and the particles are in the average size of 160 nm. In the case of ESB, cubic fluorite structure is formed after the powder is calcined at 600°C.[32,34] XRD patterns regarding the chemical compatibility between LNO and YSZ are shown in Figure 1b. No distinct reaction product is detected at a temperature below 850°C, but as the temperature increases to 900°C an electrically resistive $La_2Zr_2O_7$ phase is observed. This is consistent with the literature reports.[47–49] Thus the cell's testing temperature at 750°C and below in the present study is thermodynamically safe to avoid the chemical reaction at the interface between LNO electrode and YSZ electrolyte.

Figures 1c–1f show the SEM images of as prepared pristine LNO and LNO-ESB composite electrodes after heat-treatment at 750°C for 30 min. The surface of LNO electrode is characterized by a porous structure with loosely connected particles (Figure 1c). The particles are in the average size of 235 nm, greater than 160 nm of as synthesized powder (see Figure 1a). By contrast, the surface microstructure of LNO-ESB electrode is more compact, and the electrode structure is slightly coarsened with an average particle size of 300 nm (Figure 1d). ESB and LNO particles are representatively indicated in Figure 1d (see the arrows), as confirmed by the EDS spectra (Figure 1g). Compared to the LNO electrode (Figure 1e), the LNO-ESB electrode shows more intimate interfacial contact with the YSZ electrolyte (Figure 1f), consistent with the microstructure compactness of LNO-ESB (see Figure 1d).

Initial electrochemical performance.—After the anodes were completely reduced at 750°C for 1 h, the electrochemical performance such as polarization curves and impedance spectra were tested and the results are shown in Figure 2. The open circuit voltage of both cells is ~1.1 V, very close to the theoretical value. In the case of the cell with pristine LNO cathode (LNO cell), the peak power density (PPD) at 750°C is only 115 mW cm^{-2} (Figure 2a), close to that of the pristine LNO cells reported in literature (see Table I). The low output performance is due to the high total cell resistance (R_T) of 2.55 Ω cm^2, comprising of a cell ohmic resistance (R_Ω) of 1.13 Ω cm^2 and an electrode polarization resistance (R_P) of 1.42 Ω cm^2 (Figure 2b). R_Ω and R_T are derived from the high and low-frequency intercepts of Nyquist plots, respectively, and R_P the difference between R_T and R_Ω. R_Ω of 1.13 Ω cm^2 is drastically greater than that of 0.27 and 0.56 Ω cm^2 for identical YSZ film cells with LSCF and $LaCoO_{3-\delta}$ (LC) electrodes assembled by the identical approach,[43,44] respectively. Hidenbrand et al. also reported the increase of overall ohmic resistance using LNO electrode.[24]

On the other hand, the performance of LNO is remarkably enhanced by the incorporation of ESB. PPD of LNO-ESB cell reaches 688 mW cm^{-2} (Figure 2a), much higher than that of LNO cell. The performance enhancement is due to the significant decrease of internal resistances. R_Ω and R_P of LNO-ESB cell are 0.16 and 0.40 Ω cm^2, respectively (Figure 2b), much smaller than 1.13 and 1.42 Ω cm^2 in the case of LNO cell. R_Ω mainly contains electrolyte ohmic resistance as well as contact resistance at the interfaces between electrolyte and electrodes. As LNO cell and LNO-ESB cell have different cathodes only, the decrease of R_Ω by ESB incorporation is probably attributed to the decrease of contact resistance at the cathode/electrolyte interface. This is consistent with the enhanced interfacial contact between LNO-ESB electrode and YSZ electrolyte (see Figure 1f).

It is worthwhile noting that the decrease of R_P by ESB incorporation is mainly on the impedance arcs at frequencies above 10 Hz, while the low-frequency arcs below 10 Hz remain unchanged (Figures 2b and 2c). It is well accepted the low-frequency impedance arcs are related to gas diffusion and conversion in anode.[52–54] Consistently, we observed the low-frequency arcs are greatly affected by varying the atmospheres in anode.[55–57] On the other hand, the impedance arcs at higher frequencies are associated with the electrode processes at cathode as well as the electrochemical process at anode.[52–54,58–60] Here, the Bode plot of LNO cell shows two visible electrode processes at summit frequencies of 10^3–10^4 Hz and 10^4–10^5 Hz (Figure 2c). Both the electrode processes undergo a dramatic decrease by the ESB incorporation, and also the electrode process at the summit frequency of 10^3–10^4 Hz is shifted to 10^2–10^3 Hz. This indicates these electrode processes arise from the cathode side, most likely relating to ion migration process at the electrode/electrolyte interfaces and surface exchange reaction.[18,24,61] The variation of impedance arcs induced by polarization is in excellent agreement with our previous studies based on identical YSZ film cells with different cathode materials.[32–34,43,44]

The impedance spectra are thus fitted using an equivalent circuit with three R_iQ_i (i = H, M and L) elements where Q is a constant phase element (CPE), along with a R_Ω and an inductor L (Figure 2d). The admittance (Y) of Q is defined as

$$Y = Y_0(j\omega)^n \quad [1]$$

where Y_0 and n are the amplitude and exponent component of CPE, respectively, and ω is the angular frequency. The fitting results are listed in Tables II and III. As discussed above, the R_HQ_H and R_MQ_M elements at high and medium-frequencies are mainly related to the ion migration and surface exchange processes in cathode, respectively, while the R_LQ_L element at low frequencies is associated with the gas diffusion and conversion in anode. The substantially greater Y_0 values of Q_L compared to those of Q_H and Q_M confirm the assignment of proper electrode processes discussed above.[62,63] It is evident that the incorporation of ESB leads to the reduction of R_M and in particular R_H. R_H and R_M of LNO cell are 0.75 and 0.43 Ω cm^2, respectively (Table II), and dramatically decrease to 0.066 and 0.26 Ω cm^2 for LNO-ESB cell (Table III). The remarkable reduction of R_H is due to the facilitated ion migration as a result of enhanced interfacial contact as discussed above. Researches also observed the compact LNO interfacial layer enhances the oxygen ion transfer process as well as mass transport and charge transfer processes.[13,24–26] The reduction of R_M is ascribed to the enhanced oxygen surface exchange process due to the excellent oxygen surface exchange ability of ESB.

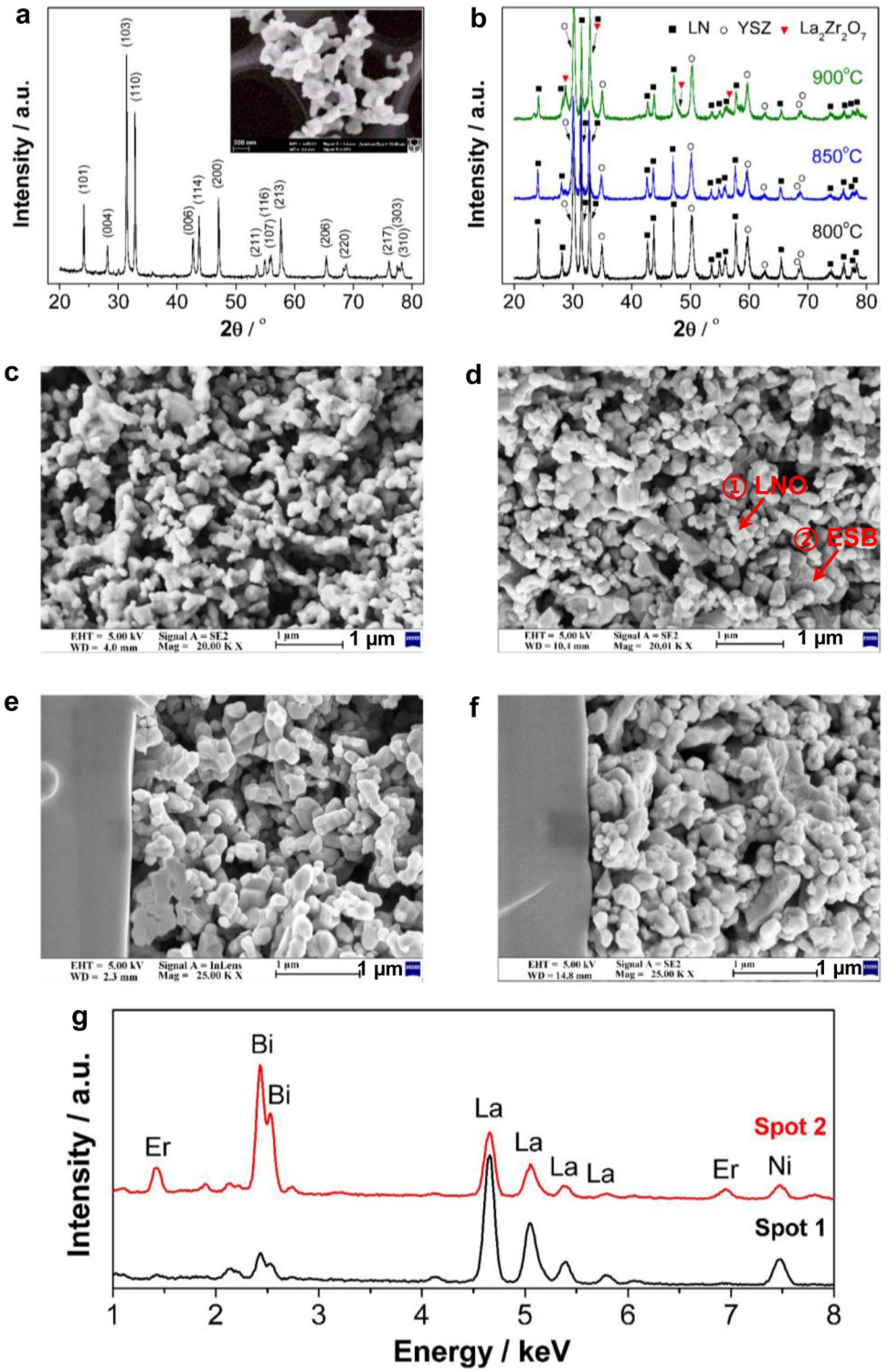

Figure 1. (a) XRD patterns and SEM image of as-synthesized LNO powder, (b) XRD patterns of LNO-YSZ mixtures heat-treated at 800–900°C, SEM images of outermost surfaces and cross sections of (c and e) LNO electrode and (d and f) LNO-ESB electrode, and (g) EDS spectra on the surfaces of LNO-ESB electrode as indicated in (d).

Operating stability.—Figure 3 shows the performance curves of LNO cell during polarization at 0.1 A cm^{-2} and 750°C. In contrast to the remarkable promotional effect of electrochemical polarization on the performance of cobaltite and manganite cathodes in our previous studies,[43,44,64–66] the polarization has an adverse effect on the LNO cell. It is evident the cell output performance decreases continuously with increasing the polarization time (Figure 3a). After polarization for 20 h, the voltage at 0.1 A cm^{-2} decreases drastically from 0.82 to 0.58 V (Figure 3b). Consistently, R_T increases gradually from 2.55 to 4.62 Ω cm^2 after polarization for 20 h (Figure 3c). In the early stage of polarization up to 4 h, R_Ω increases, but R_P slightly reduces. As the polarization time is extended, R_P increases, but R_Ω remains stable and even reduces after polarization for 20 h. The increase of R_P is primarily on both the impedance arcs with summit frequencies at 10^3–10^4 Hz

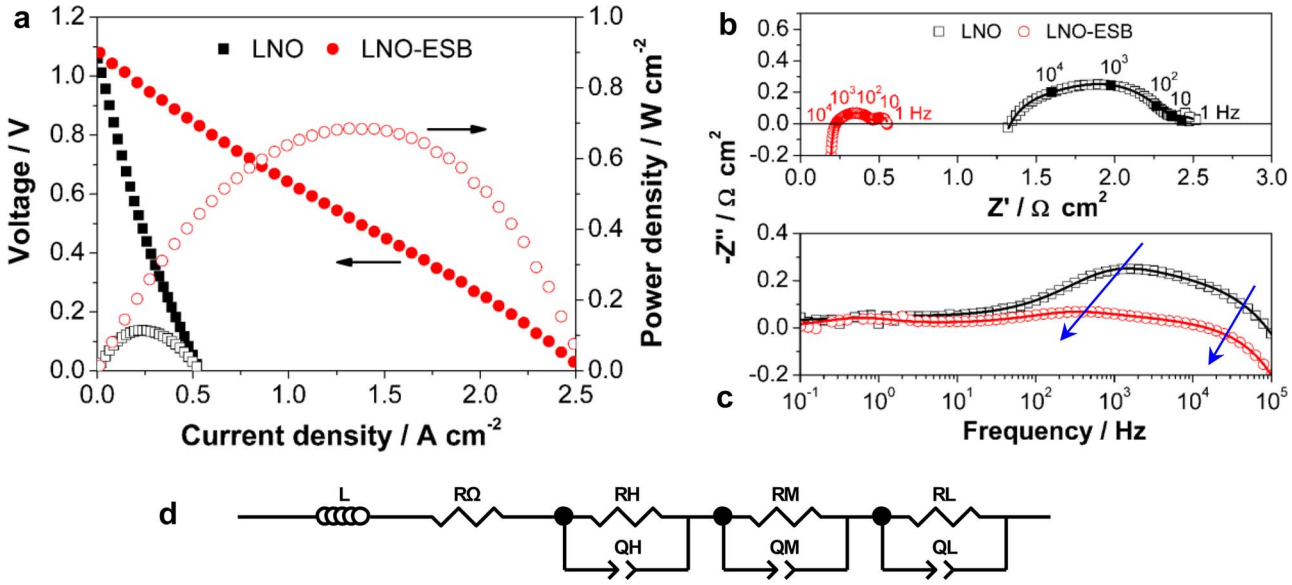

Figure 2. (a) I-V and I-P curves, (b) Nyquist plots, (c) Bode plots, and (d) equivalent circuit of LNO cell and LNO-ESB cell tested at 750°C before the polarization. In (b and c), symbols are experimental data and lines are fitted data.

Table I. Peak power densities (PPD) of LNO based cells in literature and present work.

Cell structure	Temperature/°C	PPD/mW cm^{-2}	References
Ni-YSZ/YSZ film (10 μm)/GDC (<1 μm)/LNO	800	1250	82
	750	815	
	700	485	
Ni-SDC/SDC/LSGM pellet (0.4 mm)/LNO	800	226	14
	750	160	
Ni-SDC/YSZ film (11 μm)/SDC (4 μm)/LNO	800	500	83
Ni-YSZ/YSZ film (8 μm)/LNO/LSC	800	300	29
Ni-YSZ/YSZ film (10 μm)/GDC (1.3 μm)/LNO	700	60-76	15
Ni-YSZ/YSZ film (12 μm)/LNO	750	115	This work
Ni-YSZ/YSZ film (8 μm)/LNO-SDC/LSC	800	2200	29
Ni-YSZ/YSZ film (15 μm)/LNO nanorods on YSZ scaffold	700	575	18
Ni-YSZ/YSZ film (12 μm)/LNO-ESB	750	852	This work
	700	563	
Ni-YSZ/YSZ film (20 μm)/LNO infiltrated YSZ	750	717	16
Ni-YSZ/YSZ film (8 μm)/LNO-SDC/LNO	800	400	29
Ni-SDC/SDC pellet (0.35 mm)/LNO-$L_3N_2O_7$-LDC, co-synthesized cathode	800	253	84
Ni-SDC/SDC pellet (0.35 mm)/LNO-LDC, co-synthesized cathode	800	140	30

LDC: $Ce_{0.55}La_{0.45}O_{2-\delta}$, $L_3N_2O_7$: $La_3Ni_2O_{7-\delta}$, LSC: $La_{0.7}Sr_{0.3}CoO_3$, LSGM: $La_{0.9}Sr_{0.1}Ga_{0.8}Mg_{0.2}O_{2.85}$.

Table II. Resistances derived by fitting the impedance spectra of LNO cell during stability test at 0.1 A cm^{-2} and 750°C.

			High-frequency arc, R_HQ_H			Medium-frequency arc, R_MQ_M			Low-frequency arc, R_LQ_L		
Time/h	L/×10^{-6} H	R_Ω/Ω cm^2	R_H/Ω cm^2	Y_{0H}/×10^{-3} F cm^{-2}	n_H	R_M/Ω cm^2	Y_{0M}/×10^{-3} F cm^{-2}	n_M	R_L/Ω cm^2	Y_{0L}/F cm^{-2}	n_L
0	1.13	1.13	0.75	3.84	0.51	0.43	3.00	0.77	0.24	1.83	0.42
4	0.93	1.43	0.74	2.90	0.49	0.36	1.77	0.80	0.26	0.87	0.32
8	0.95	1.46	1.18	1.56	0.52	0.46	2.33	0.70	0.35	0.39	0.44
20	1.43	1.02	1.59	0.41	0.60	1.46	2.18	0.66	0.55	0.26	0.60

Table III. Resistances derived by fitting the impedance spectra of LNO-ESB cell during stability test at 0.5 A cm^{-2} and 750°C.

			High-frequency arc, R_HQ_H			Medium-frequency arc, R_MQ_M			Low-frequency arc, R_LQ_L		
Time/h	L/×10^{-6} H	R_Ω/Ω cm^2	R_H/Ω cm^2	Y_{0H}/×10^{-3} F cm^{-2}	n_H	R_M/Ω cm^2	Y_{0M}/F cm^{-2}	n_M	R_L/Ω cm^2	Y_{0L}/F cm^{-2}	n_L
0	1.53	0.16	0.066	13.3	0.93	0.26	0.112	0.40	0.072	3.96	0.99
20	1.53	0.12	0.071	9.48	0.92	0.20	0.090	0.41	0.083	4.32	0.86
100	1.53	0.15	0.072	5.61	0.96	0.20	0.048	0.44	0.072	6.65	0.66
200	1.50	0.20	0.080	14.0	0.84	0.21	0.038	0.46	0.071	4.06	0.95

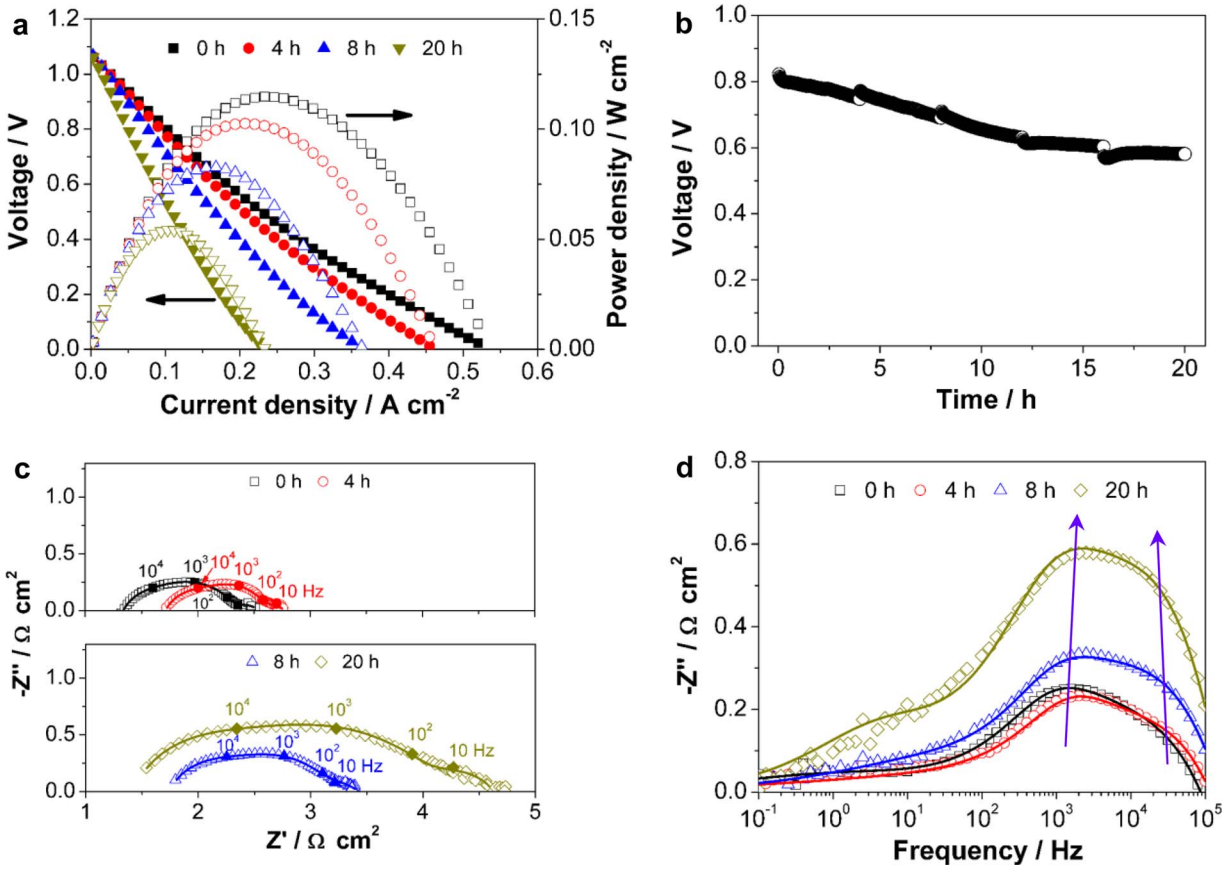

Figure 3. Performance curves of LNO cell as a function of polarization time at 0.1 A cm^{-2} and 750°C. (a) Polarization curves, (b) stability curves, (c) Nyquist plots, and (d) Bode plots. In (c and d), symbols are experimental data and lines are fitted data using the equivalent circuit in Fig. 2d.

and 10^4–10^5 Hz (Figures 3c, 3d and Table II), related to the aforementioned electrode processes at cathode. These observations imply the electrochemical polarization has a detrimental effect on the interfacial conductivity and electrocatalytic activity of the LNO electrode.

On the other hand, the LNO-ESB cell has enhanced operating stability during polarization at 0.5 A cm^{-2} and 750°C for 20 h, and the performance curves are shown in Figure 4. After polarization for 20 h, PPD increases from 688 to 852 mW cm^{-2} (Figure 4a). R_Ω and R_P after polarization for 20 h are 0.12 and 0.35 Ω cm^2 respectively (Figure 4b), smaller than 0.16 and 0.40 Ω cm^2 before the polarization. It is evident from the fitting results that the decrease of R_P is primarily caused by R_M. Initial R_M is 0.26 Ω cm^2 and decreases to 0.20 Ω cm^2 after polarization for 20 h. The decrease of R_Ω and R_M indicates that the performance enhancement is probably due to the enhanced interfacial contact and electrocatalytic activity of the LNO-ESB cathode by the polarization.

After polarization at 0.5 A cm^{-2} and 750°C for 20 h, the cell's polarization curves were tested at different temperatures. PPDs are 852, 563, 327 and 173 mW cm^{-2} at 750, 700, 650 and 600°C, respectively (Figure 4c). The performances are comparable with those of the cells using LNO-based composite cathodes in literature (see Table I). The activation energy derived from the temperature-dependent R_P plots is ~91 kJ mol^{-1} (Figure 4d).

To estimate the operating stability over an extended period, the LNO-ESB cell was operated at 0.5 A cm^{-2} and 750°C for 200 h and the stability curves are shown in Figure 5. After the increase of voltage in the early stage of polarization for 20 h, the cell undergoes a slow loss of voltage by further polarization up to 200 h, but it is still much more stable than the LNO cell (Figure 5a). The performance loss of LNO-ESB cell is mainly due to the increase of R_Ω, as R_P remains stable (Figure 5b and Table III). R_Ω is 0.12 Ω cm^2 after polarization for 20 h and gradually increases to 0.20 Ω cm^2 after polarization for 200 h. This may imply the deterioration of electrode/electrolyte interface during the stability tests. The reason for the stable R_P is unclear at the present stage. Nevertheless, the stability of R_P of LNO-ESB cell again proves the performance loss of LNO cell arises from the cathode (see Figure 3).

Microstructural and elemental analysis.—Figure 6 shows the SEM images and SIMS analysis of the YSZ electrolyte surfaces of LNO cell after polarization at 0.1 A cm^{-2} and 750°C for 20 h. Another LNO cell heat-treated at 750°C for 20 h under open circuit conditions was also prepared for comparison. The LNO electrodes were partly peeled off by adhesive tape. There is a porous thin layer formed in particular at grain boundary regions of YSZ surface after polarization (Figure 6a), in contrast to the relatively clean YSZ surface after heat-treatment under open circuit conditions (Figure 6b). Depth profiles analysis indicates that the thin surface layer is rich in La, and the thickness is ~40 nm (Figure 6c). It is to note that the absence of Ni in the depth profiles is due to its low ionisation rate. After the SIMS analysis, a rectangular pit in a depth of ~90 nm is observed (see Figure S1a, Supplemental Material). SIMS imaging on the pit reveals that La preferentially distributes at the YSZ grain boundaries (Figure 6d), indicating the accumulated La element diffuses certain depth into the electrolyte along the grain boundaries. The driving force is most likely the chemical affinity between La and Zr to form $La_2Zr_2O_7$ under the influence of cathodic polarization, and the reaction is favored at the active, defective grain boundaries. The exaction of La from LNO and its reaction with YSZ is probably responsible for the poor operating stability of LNO cell (see Figure 3).

Figure 7 shows the SEM images and SIMS analysis of the YSZ electrolyte surfaces of LNO-ESB cell after polarization at 0.5 A cm^{-2} and 750°C. After polarization for 20 h, the LNO-ESB cathode is in excellent contact with the YSZ electrolyte (Figure 7a and S2,

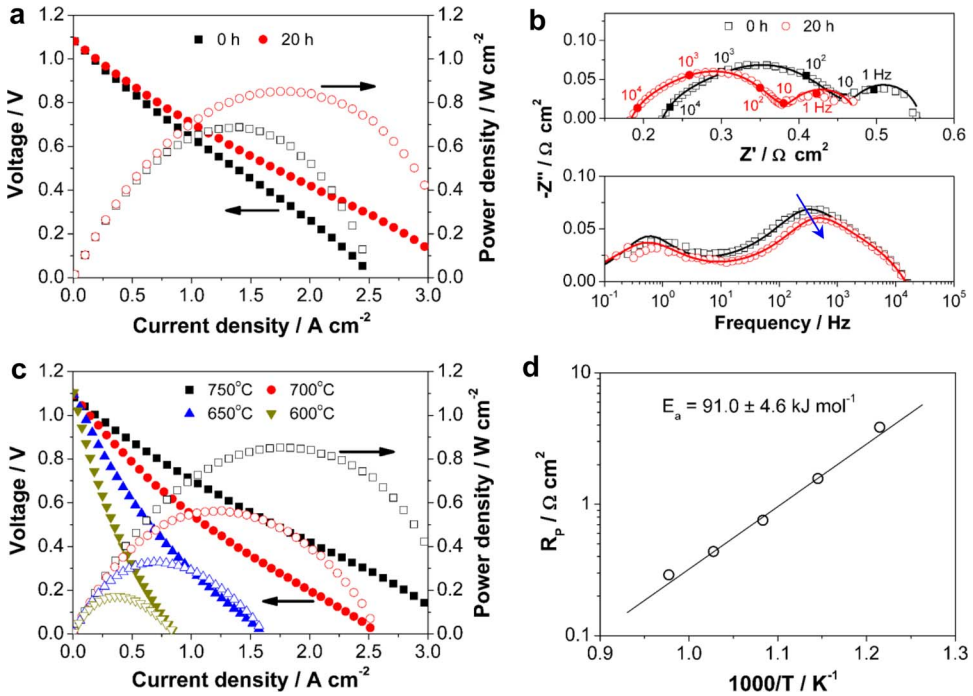

Figure 4. Performance curves of LNO-ESB cell as a function of polarization time at 0.5 A cm^{-2} and 750°C. (a) Polarization curves, (b) Nyquist and Bode plots; symbols are experimental data and lines are fitted data, (c) I-V and I-P curves at different temperatures, and (d) activation energy plot. Prior to the test of (c and d), the cell was polarized at 0.5 A cm^{-2} and 750°C for 20 h.

Supplemental Material), consistent with the performance enhancement during the course of polarization (see Figure 4). After polarization for 50 h, the YSZ surface is relatively clean with several remaining particles (Figure 7b), very different to the presence of the distinct deposition layer after the LNO cell was polarized for a shorter period of 20 h (see Figure 6a). However, a porous thin surface layer is observable after extending the polarization time to 200 h (Figure 7c). This layer is determined to be La-rich in a thickness of ~30 nm (Figure 7d), thinner than the La-rich layer of LNO cell after polarization for a much shorter period of 20 h. In addition, there is no sign of accumulation of La at the YSZ grain boundaries after the depth profiling measurements (Figure 7e), in contrast to the case of LNO cell (see Figure 6d). In Figure 7e, the bright spots arise from the remaining LNO particles (see Figure S1b, Supplemental Material). Thus, it is evident that the presence of ESB remarkably mitigates the extent of extraction of La from LNO lattice and its accumulation on the YSZ surface. Nevertheless, the extraction of La, even in lesser extent, would lead to partial decomposition of LNO and formation of a resistive $La_2Zr_2O_7$ layer, reducing the contact conductivity at the electrode/electrolyte interface and thereby a gradual increase of R_Ω (see Figure 5b).

Proposed mechanism of enhanced stability of LNO-ESB.—La surface segregation in LNO has been reported.[67–70] For example, Skinner et al. investigated the surface chemistry and restructuring in LNO film using low energy ion scattering and observed preferential La segregation on the outmost surface of LNO accompanied by Ni-enrichment below the surface.[70] The presence of surface segregated La species and its chemical affinity with Zr to form $La_2Zr_2O_7$ is most likely attributed to the chemical incompatibility between LNO and YSZ at 900°C (see Figure 1b). Here, it appears that the cathodic polarization has a critical effect on accelerating the La surface segregation and migration to the YSZ surfaces, as is evident by the observation of a distinct La-rich layer on the YSZ surfaces after polarization at 750°C for 20 h (Figure 6a), in contrast to the much cleaner YSZ surface after heat-treatment at open circuit under identical conditions (Figure 6b).

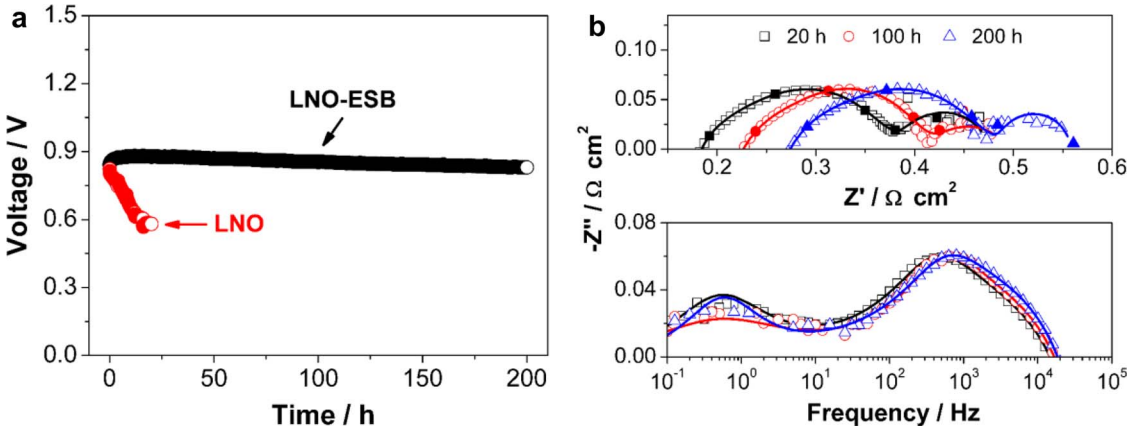

Figure 5. (a) Stability curve, (b) Nyquist and Bode plots of LNO-ESB cell at 0.5 A cm^{-2} and 750°C. In (a), the stability curve of LNO cell at 0.1 A cm^{-2} and 750°C is also plotted for comparison. In (b), symbols are experimental data and lines are fitted data using the equivalent circuit in Fig. 2d.

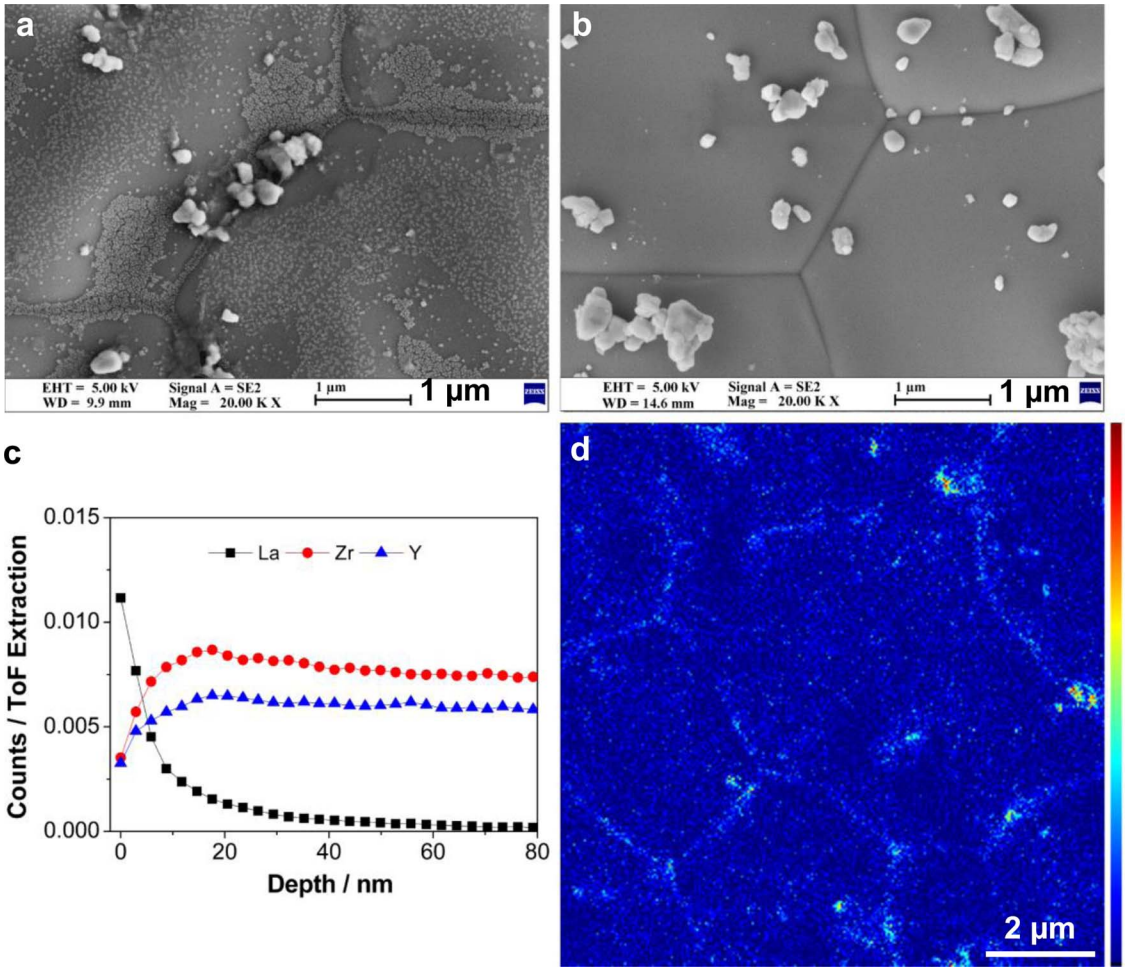

Figure 6. SEM images of exposed YSZ electrolyte surfaces of LNO cell after heat-treatment at 750°C for 20 h: (a) polarization at 0.1 A cm^{-2} and (b) under open circuit conditions. (c) SIMS depth profiles and (d) elemental map of La after the depth profiling measurements of the YSZ surface shown in (a).

Recent studies have shown that the electrochemical polarization has a significant impact on the mobility of surface segregated Sr cations.[71–77] In the case of MIEC LSCF electrode assembled on YSZ electrolyte, we observed cathodic polarization has an accelerating effect on the Sr segregation and migration from LSCF to YSZ surface, leading to rapid performance degradation.[43] For the electronically conducting Sr-free LC electrode assembled on YSZ electrolyte, partial surface demixing and formation of Co and La-rich particles occurs at the electrode/electrolyte interface after cathodic polarization; on the other hand, the addition of GDC to form a LC-GDC composite cathode remarkably enhances the performance and structural stability of LC.[44] These results imply that the cathodic potential may be a key driving force for accelerating the diffusion and migration A-site cations from the Co-containing cathodes studied. Moreover, a number of in situ experiments reveal that strong cathodic polarization also induces partial reduction of B-site cations or variation of unit cell volume of perovskite oxides such as LSM and $La_{0.6}Sr_{0.4}CoO_{3-\delta}$.[78–80] However, there is lack of relevant studies regarding effect of polarization on LNO electrode.

As an attempt to interpret the promotional effect of ESB incorporation, we hypothesize that the cation stability of LNO electrode is also dependent on the level of cathodic potential. The high cathodic potential (Figure S3, Supplemental Material) may increase the activity of La cations in the LNO lattice. On the contrary, the presence of ESB leads to a dramatic decrease of cathodic potential of LNO electrode (Figure S3, Supplemental Material), providing a much less driving force for the segregation and accumulation of La cations (see Figure 7) and therefore enhances the cell operating stability (see Figure 5). The operating stability could be further improved by deposition of a GDC barrier layer on YSZ electrolyte.[81]

Conclusions

ESB has been incorporated to LNO and assembled on YSZ electrolyte by a facile electrochemical polarization approach. The presence of ESB remarkably enhances the microstructure compactness of LNO electrode, leading to a significantly reduced contact resistance at the electrode/electrolyte interface and enhanced electrocatalytic activity. The LNO-ESB cell generates a peak power density of 852 mW cm^{-2} at 750°C, substantially higher than 115 mW cm^{-2} of LNO cell. The presence of ESB also significantly enhances the operating stability of LNO at 750°C in the duration period of 200 h studied, due to the mitigated extraction and migration of La from LNO to YSZ electrolyte. The present work fundamentally sheds light on the feasibility of application of layered nickelate cathodes on YSZ electrolyte, but great efforts are needed to enhance the cation stability at the electrode/electrolyte interface.

Acknowledgments

The project was supported by National Natural Science Foundation of China (21875038), Natural Science Foundation of Fujian Province, China (2018J01678). Minle Chen, Yuanfeng Zou and Lizhen Jiang from College of Materials Science and Engineering, Fuzhou University are acknowledged for conducting the chemical compatibility experiments and preparing SEM samples. The authors acknowledge the

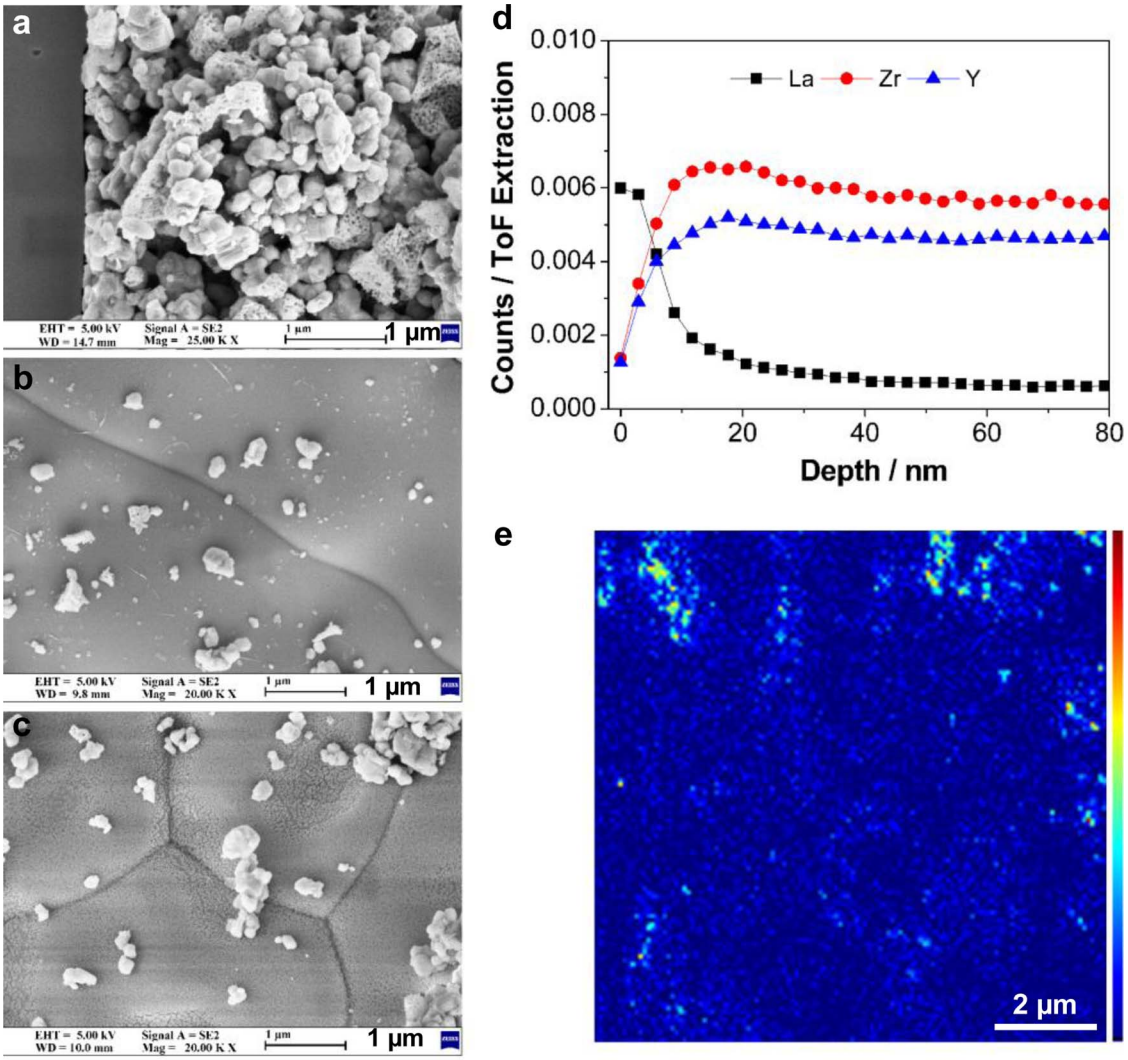

Figure 7. Morphologies and elemental analysis of LNO-ESB cell after polarization at 0.5 A cm^{-2} and 750°C for (a) 20 h, (b) 50 h and (c-e) 200 h. SEM images of (b) cross section of fractured cell and (b and c) exposed YSZ electrolyte surfaces. (d) SIMS depth profiles and (e) elemental map of La after the depth profiling measurements on the YSZ surface shown in (c).

facilities, scientific and technical assistance of the Curtin University Microscopy, which is funded by the University, State and Commonwealth Governments.

ORCID

San Ping Jiang https://orcid.org/0000-0002-7042-2976
Kongfa Chen https://orcid.org/0000-0001-7809-675X

References

1. Y. Chen, W. Zhou, D. Ding, M. Liu, F. Ciucci, M. Tade, and Z. Shao, *Advanced Energy Materials*, **5**, 1500537 (2015).
2. C. W. Sun, R. Hui, and J. Roller, *Journal of Solid State Electrochemistry*, **14**, 1125 (2010).
3. A. Jun, J. Kim, J. Shin, and G. Kim, *ChemElectroChem*, **3**, 511 (2015).
4. V. V. Kharton, A. P. Viskup, E. N. Naumovich, and F. M. B. Marques, *Journal of Materials Chemistry*, **9**, 2623 (1999).
5. S. J. Skinner and J. A. Kilner, *Solid State Ionics*, **135**, 709 (2000).
6. A. Tarancon, M. Burriel, J. Santiso, S. J. Skinner, and J. A. Kilner, *Journal of Materials Chemistry*, **20**, 3799 (2010).
7. X. Zhang, H. Zhang, and X. Liu, *Journal of Power Sources*, **269**, 412 (2014).
8. Y. Li, S.-L. Zhang, C.-X. Li, T. Wei, G.-J. Yang, C.-J. Li, and M. Liu, *Journal of Thermal Spray Technology*, **25**, 392 (2016).
9. W. Zhou, F. L. Liang, Z. P. Shao, and Z. H. Zhu, *Scientific Reports*, **2**, 327 (2012).
10. J. Li, J. Li, D. Yan, J. Pu, B. Chi, and L. Jian, *Electrochimica Acta*, **270**, 294 (2018).
11. S. P. Jiang and X. Chen, *International Journal of Hydrogen Energy*, **39**, 505 (2014).
12. S.-N. Lee, A. Atkinson, and J. A. Kilner, *ECS Transactions*, **57**, 605 (2013).
13. R. Sayers, M. Rieu, P. Lenormand, F. Ansart, J. A. Kilner, and S. J. Skinner, *Solid State Ionics*, **192**, 531 (2011).
14. M. J. Escudero, A. Fuerte, and L. Daza, *Journal of Power Sources*, **196**, 7245 (2011).
15. J. Fondard, P. Bertrand, A. Billard, S. Fourcade, P. Batocchi, F. Mauvy, G. Bertrand, and P. Briois, *Solid State Ionics*, **310**, 10 (2017).
16. S. Choi, S. Yoo, J.-Y. Shin, and G. Kim, *Journal of the Electrochemical Society*, **158**, B995 (2011).
17. C. Nicollet, A. Flura, V. Vibhu, A. Rougier, J. M. Bassat, and J. C. Grenier, *Journal of Power Sources*, **294**, 473 (2015).
18. J. S. A. Carneiro, R. A. Brocca, M. L. R. S. Lucena, and E. Nikolla, *Applied Catalysis B: Environmental*, **200**, 106 (2017).
19. J. Railsback and S. A. Barnett, *Journal of Power Sources*, **395**, 1 (2018).
20. C. Solís, L. Navarrete, and J. M. Serra, *Journal of Power Sources*, **240**, 691 (2013).
21. V. Vibhu, A. Rougier, C. Nicollet, A. Flura, J.-C. Grenier, and J.-M. Bassat, *Solid State Ionics*, **278**, 32 (2015).
22. S. Li, H. Tu, F. Li, M. T. Anwar, and L. Yu, *Journal of Alloys and Compounds*, **694**, 17 (2017).
23. Z. Zhu, M. Li, C. Xia, and H. J. M. Bouwmeester, *Journal of Materials Chemistry A*, **5**, 14012 (2017).
24. N. Hildenbrand, P. Nammensma, D. H. A. Blank, H. J. M. Bouwmeester, and B. A. Boukamp, *Journal of Power Sources*, **238**, 442 (2013).
25. M. Benamira, A. Ringuedé, M. Cassir, D. Horwat, P. Lenormand, F. Ansart, J. M. Bassat, and J. P. Viricelle, *Journal of Alloys and Compounds*, **746**, 413 (2018).
26. R. J. Woolley and S. J. Skinner, *Solid State Ionics*, **255**, 1 (2014).
27. R. J. Woolley and S. J. Skinner, *Journal of Power Sources*, **243**, 790 (2013).
28. J. Hou, Z. Zhu, J. Qian, and W. Liu, *Journal of Power Sources*, **264**, 67 (2014).
29. C. Laberty, F. Zhao, K. E. Swider-Lyons, and A. V. Virkar, *Electrochemical and Solid-State Letters*, **10**, B170 (2007).

30. P. Li, Z. Wang, X. Huang, L. Zhu, Z. Cao, Y. Zhang, B. Wei, X. Zhu, and Z. Lü, *Journal of Alloys and Compounds*, **705**, 105 (2017).
31. E. D. Wachsman and K. T. Lee, *Science*, **334**, 935 (2011).
32. N. Ai, N. Li, S. He, Y. Cheng, M. Saunders, K. Chen, T. Zhang, and S. P. Jiang, *Journal of Materials Chemistry A*, **5**, 12149 (2017).
33. N. Ai, J.-P. Veder, Y. Cheng, M. Chen, K. Chen, T. Zhang, and S. P. Jiang, *Journal of The Electrochemical Society*, **164**, F1471 (2017).
34. N. Ai, M. Chen, S. He, K. Chen, T. Zhang, and S. P. Jiang, *Journal of Materials Chemistry A*, **6**, 6510 (2018).
35. M. Chen, Y. Cheng, S. He, N. Ai, J.-P. Veder, W. D. A. Rickard, M. Saunders, K. Chen, T. Zhang, and S. P. Jiang, *Journal of Power Sources*, **397**, 16 (2018).
36. S. He, Q. Zhang, G. Maurizio, L. Catellani, K. Chen, Q. Chang, M. Santarelli, and S. P. Jiang, *ACS applied materials & interfaces*, **10**, 40549 (2018).
37. J. W. Park, D. W. Joh, B.-H. Yun, K. J. Samdani, and K. T. Lee, *International Journal of Hydrogen Energy*, **42**, 6332 (2017).
38. J. W. Park and K. T. Lee, *Journal of Industrial and Engineering Chemistry*, **60**, 505 (2018).
39. Z. Y. Jiang, C. R. Xia, F. Zhao, and F. L. Chen, *Electrochemical and Solid State Letters*, **12**, B91 (2009).
40. K. T. Lee, A. A. Lidie, H. S. Yoon, and E. D. Wachsman, *Angewandte Chemie International Edition*, **49**, 13463 (2014).
41. J. Yan, Z. Zhao, L. Shang, D. Ou, and M. Cheng, *Journal of Power Sources*, **319**, 124 (2016).
42. K. Chen, N. Li, N. Ai, M. Li, Y. Cheng, W. D. A. Rickard, J. Li, and S. P. Jiang, *Journal of Materials Chemistry A*, **4**, 17678 (2016).
43. K. Chen, N. Li, N. Ai, Y. Cheng, W. D. A. Rickard, and S. P. Jiang, *ACS Applied Materials & Interfaces*, **8**, 31729 (2016).
44. N. Ai, N. Li, W. D. Rickard, Y. Cheng, K. Chen, and S. P. Jiang, *ChemSusChem*, **10**, 993 (2017).
45. S. He, K. Chen, M. Saunders, Z. Quadir, S. Tao, J. T. S. Irvine, C. Q. Cui, and S. P. Jiang, *Solid State Ionics*, **325**, 176 (2018).
46. S. He, M. Saunders, K. Chen, H. Gao, A. Suvorova, W. D. A. Rickard, Z. Quadir, C. Q. Cui, and S. P. Jiang, *Journal of The Electrochemical Society*, **165**, F417 (2018).
47. A. M. Hernández, L. Mogni, and A. Caneiro, *International Journal of Hydrogen Energy*, **35**, 6031 (2010).
48. A. Montenegro-Hernandez, J. Vega-Castillo, L. Mogni, and A. Caneiro, *International Journal of Hydrogen Energy*, **36**, 15704 (2011).
49. M. Ferkhi, A. Ringuedé, A. Khaled, L. Zerroual, and M. Cassir, *Electrochimica Acta*, **75**, 80 (2012).
50. J. Wang, Z. Lu, K. Chen, X. Huang, N. Ai, J. Y. Hu, Y. Zhang, and W. H. Su, *Journal of Power Sources*, **164**, 17 (2007).
51. N. Ai, Z. Lu, K. Chen, X. Huang, X. Du, and W. Su, *Journal of Power Sources*, **171**, 489 (2007).
52. R. Barfod, M. Mogensen, T. Klemenso, A. Hagen, Y.-L. Liu, and P. V. Hendriksen, *Journal of the Electrochemical Society*, **154**, B371 (2007).
53. M. Riegraf, V. Yurkiv, R. Costa, G. Schiller, and K. A. Friedrich, *ChemSusChem*, **10**, 587 (2017).
54. M. J. López-Robledo, M. A. Laguna-Bercero, A. Larrea, and V. M. Orera, *Journal of Power Sources*, **378**, 184 (2018).
55. N. Ai, S. He, N. Li, Q. Zhang, W. D. A. Rickard, K. Chen, T. Zhang, and S. P. Jiang, *Journal of Power Sources*, **384**, 125 (2018).
56. K. Chen, L. Zhang, N. Ai, S. Zhang, Y. Song, Y. Song, Q. Yi, C.-Z. Li, and S. P. Jiang, *Energy & Fuels*, **30**, 1849 (2016).
57. K. Chen, L. Zhang, M. Gholizadeh, N. Ai, M. M. Hasan, D. Mourant, C.-Z. Li, and S. P. Jiang, *Chemical Engineering Science*, **154**, 108 (2016).
58. H. Sumi, T. Yamaguchi, K. Hamamoto, T. Suzuki, and Y. Fujishiro, *Journal of Power Sources*, **226**, 354 (2013).
59. T. Yamaguchi, H. Sumi, K. Hamamoto, T. Suzuki, Y. Fujishiro, J. D. Carter, and S. A. Barnett, *International Journal of Hydrogen Energy*, **39**, 19731 (2014).
60. S.-L. Zhang, H. Wang, M. Y. Lu, C.-X. Li, C.-J. Li, and S. A. Barnett, *Journal of Power Sources*, **426**, 233 (2019).
61. B. Guan, W. Y. Li, H. Zhang, and X. B. Liu, *Journal of the Electrochemical Society*, **162**, F707 (2015).
62. R. Mohammadi, M. Ghassemi, Y. M. Barzi, and J. Pirkandi, *Journal of Solid State Electrochemistry*, **18**, 2815 (2014).
63. M. Lo Faro, R. M. Reis, G. G. A. Saglietti, V. L. Oliveira, S. C. Zignani, S. Trocino, S. Maisano, E. A. Ticianelli, N. Hodnik, F. Ruiz-Zepeda, and A. S. Arico, *Applied Catalysis B-Environmental*, **220**, 98 (2018).
64. M. Li, K. Chen, B. Hua, J.-L. Luo, W. D. A. Rickard, J. Li, J. T. S. Irvine, and S. P. Jiang, *Journal of Materials Chemistry A*, **4**, 19019 (2016).
65. S. He, K. Chen, M. Saunders, J. Li, C. Q. Cui, and S. P. Jiang, *Journal of The Electrochemical Society*, **164**, F1437 (2017).
66. N. Li, N. Ai, S. He, Y. Cheng, W. D. A. Rickard, K. Chen, T. Zhang, and S. P. Jiang, *Solid State Ionics*, **316**, 38 (2018).
67. J. Druce, H. Tellez, M. Burriel, M. D. Sharp, L. J. Fawcett, S. N. Cook, D. S. McPhail, T. Ishihara, H. H. Brongersma, and J. A. Kilner, *Energy & Environmental Science*, **7**, 3593 (2014).
68. M. Burriel, S. Wilkins, J. P. Hill, M. A. Munoz-Marquez, H. H. Brongersma, J. A. Kilner, M. P. Ryan, and S. J. Skinner, *Energy & Environmental Science*, **7**, 311 (2014).
69. J. Wu, S. S. Pramana, S. J. Skinner, J. A. Kilner, and A. P. Horsfield, *Journal of Materials Chemistry A*, **3**, 23760 (2015).
70. K.-T. Wu, H. Téllez, J. Druce, M. Burriel, F. Yang, D. McComb, T. Ishihara, J. A. Kilner, and S. J. Skinner, *Journal of Materials Chemistry A*, **5**, 9003 (2017).
71. M. Finsterbusch, A. Lussier, J. A. Schaefer, and Y. U. Idzerda, *Solid State Ionics*, **212**, 77 (2012).
72. A.-K. Huber, M. Falk, M. Rohnke, B. Luerßen, L. Gregoratti, M. Amati, and J. Janek, *Physical Chemistry Chemical Physics*, **14**, 751 (2012).
73. E. Mutoro, E. J. Crumlin, H. Pöpke, B. Luerssen, M. Amati, M. K. Abyaneh, M. D. Biegalski, H. M. Christen, L. Gregoratti, J. Janek, and Y. Shao-Horn, *The Journal of Physical Chemistry Letters*, **3**, 40 (2012).
74. M. Rohnke, M. Falk, A. K. Huber, and J. Janek, *Journal of Power Sources*, **221**, 97 (2013).
75. B. Wei, K. Chen, L. Zhao, Z. Lu, and S. P. Jiang, *Physical Chemistry Chemical Physics*, **17**, 1601 (2015).
76. C. C. Wang, K. Chen, T. Jiang, Y. Yang, Y. Song, H. Meng, S. P. Jiang, and B. Lin, *Electrochimica Acta*, **269**, 188 (2018).
77. S. Ovtar, A. Hauch, S. Veltzé, and M. Chen, *Electrochimica Acta*, **266**, 293 (2018).
78. M. Backhaus-Ricoult, *Solid State Ionics*, **177**, 2195 (2006).
79. M. Backhaus-Ricoult, K. Adib, T. St.Clair, B. Luerssen, L. Gregoratti, and A. Barinov, *Solid State Ionics*, **179**, 891 (2008).
80. I. Kivi, J. Aruväli, K. Kirsimäe, A. Heinsaar, G. Nurk, and E. Lust, *Journal of The Electrochemical Society*, **162**, F354 (2015).
81. V. Vibhu, A. Rougier, C. Nicollet, A. Flura, S. Fourcade, N. Penin, J.-C. Grenier, and J.-M. Bassat, *Journal of Power Sources*, **317**, 184 (2016).
82. Y. Lee and H. Kim, *Ceramics International*, **41**, 5984 (2015).
83. Y.-P. Wang, K. Zhao, Q. Xu, D.-P. Huang, M. Chen, and B.-H. Kim, *International Journal of Hydrogen Energy*, **43**, 4482 (2018).
84. P. Li, X. Huang, B. Wei, Z. Wang, Y. Zhang, X. Zhu, L. Zhang, L. Zhu, and Z. Lü, *International Journal of Hydrogen Energy*, **42**, 17202 (2017).